

Revision 1: Magnesiosiderite Diffraction at high P - T , AM, 7/15/2013

1 **Thermal Equation of State and Spin Transition of Magnesiosiderite at**
2 **High Pressure and Temperature**

3 Jin Liu^{1,*}, Jung-Fu Lin¹, Zhu Mao¹, Vitali B. Prakapenka²

4 ¹Department of Geological Science, Jackson School of Geosciences, The University of
5 Texas at Austin, Austin, TX 78712, USA

6 ²Consortium for Advanced Radiation Sources, The University of Chicago, Chicago, IL
7 60637, USA

8 * Email: jinliu@utexas.edu

9

10 **ABSTRACT**

11 *In situ* synchrotron X-ray diffraction experiments on natural magnesiosiderite
12 [(Mg_{0.35}Fe_{0.65})CO₃] were conducted using resistive and laser-heated diamond anvil cells
13 (DACs) up to 78 GPa and 1200 K. Based on thermal elastic modeling of the measured
14 pressure-volume curves at given temperatures, we have derived thermal equation of state
15 (EoS) parameters and the spin-crossover diagram of magnesiosiderite across the spin
16 transition. These results show the spin crossover broadened and shifted toward higher
17 pressures at elevated temperatures. Low-spin magnesiosiderite is 6% denser and 8% more
18 incompressible than the high-spin phase at 1200 K and high pressures. Within the spin
19 crossover from 53 to 63 GPa at 1200 K, magnesiosiderite exhibits anomalous thermal
20 elastic behaviors, including a dramatic increase in the thermal expansion coefficient by a

1

Revision 1: Magnesiosiderite Diffraction at high P - T , AM, 7/15/2013

21 factor of twenty and a drop in the isothermal bulk modulus and the bulk sound velocity
22 by approximately 75% and 50%, respectively. Compared with the end-member magnesite
23 [MgCO₃] at relevant pressure-temperature conditions of the subducted slabs, the high-
24 spin magnesiosiderite with 65 mole% FeCO₃ is approximately 21-23% denser and its unit
25 cell volume is 2-4% larger, whereas the low-spin state is 28-29% denser and 2% smaller
26 than the end-member magnesite. Since ferromagnesite with 20 mole% of iron has been
27 proposed to be a potential deep-carbon carrier, our results here indicate that the dense
28 low-spin ferromagnesite can become more stable than high-spin ferromagnesite at
29 pressures above approximately 50 GPa, providing a mechanism for (MgFe)-bearing
30 carbonate to be a major carbon host in the deeper lower mantle.

31 **Keywords:** Fe-rich carbonate, thermal equation of state, spin transition,
32 ferromagnesite, diamond anvil cell

33

34 INTRODUCTION

35 The existence of oxidized carbon in the Earth's deep interior can significantly affect a
36 number of geophysical and geochemical properties of the planet (e.g., Gaillard et al. 2008;
37 Dasgupta and Hirschmann 2010). Due to the nominally low solubility of carbon in the
38 main minerals of the mantle (Keppler et al. 2003; Dasgupta et al. 2013), carbon from
39 primordial origins or altered ocean crusts is expected to be present as accessory phases in
40 the deep mantle, such as carbonates, carbonate melts, carbon bearing fluids, diamond,
41 and/or iron carbides (e.g., Berg 1986; Alt and Teagle 1999; Pal'yanov et al. 1999).
42 Laboratory studies of carbon-bearing minerals at high pressures and temperatures (P - T)

2

Revision 1: Magnesiosiderite Diffraction at high P - T , AM, 7/15/2013

43 can provide crucial constraints on the role and behavior of deep carbon in the
44 geochemistry and geophysics of the Earth's mantle, and therefore the mantle's role in the
45 global carbon cycle (Hazen et al. 2012). Magnesite [MgCO_3] has been reported to be
46 stable at relevant P - T conditions of the Earth's lower mantle (Isshiki et al. 2004; Oganov
47 et al. 2008). High P - T experiments on carbonated peridotite and eclogite further showed
48 that approximately 20 mole% siderite [FeCO_3] can be dissolved in magnesite, forming an
49 Fe-bearing [(MgFe) CO_3] solid solution with rhombohedral structure (Dasgupta et al.
50 2004). This form, called ferromagnesite for the Mg-rich part of the system and
51 magnesiosiderite for the Fe-rich part of the system, could be a stable major deep-carbon
52 host in the lower mantle.

53 Iron as a transition metal is known to play an important role in the physical, chemical,
54 and transport properties of the mantle minerals due to the various electronic spin and
55 valence states exhibited by the $3d$ electrons of iron at high P - T conditions (e.g., Lin and
56 Tsuchiya 2008). An electronic high-spin (HS) to low-spin (LS) transition of iron in the
57 magnesite-siderite system has been recently observed to occur at approximately 45 GPa
58 using a number of experimental and theoretical techniques including the high-pressure X-
59 ray emission spectroscopy, X-ray diffraction, laser Raman spectroscopy, and first-
60 principles calculations (Mattila et al. 2007; Shi et al. 2008; Lavina et al. 2009, 2010a,
61 2010b; Nagai et al. 2010; Farfan et al. 2012; Lin et al. 2012). This transition is associated
62 with a 6-10% reduction in the unit-cell volume, making the LS state denser and more
63 incompressible than the HS counterpart (Lavina et al. 2009, 2010b; Nagai et al. 2010;
64 Farfan et al. 2012; Lin et al. 2012). It has been suggested that iron may preferentially
65 partition into the LS ferromagnesite, which would make it a stable deep-carbon host in

Revision 1: Magnesiosiderite Diffraction at high P - T , AM, 7/15/2013

66 the lower mantle (Lavina et al. 2009, 2010a, 2010b; Nagai et al. 2010; Farfan et al. 2012;
67 Lin et al. 2012). On the other hand, iron-bearing magnesite and siderite have been
68 reported to transform into an assemblage of magnetite, nano-diamonds, and a new high-
69 pressure phase with three-membered rings of corner-sharing $(\text{CO}_4)^{4-}$ tetrahedra at
70 pressures exceeding 40 GPa and high temperatures (Boulard et al. 2011, 2012).
71 Furthermore, the electronic spin-pairing transition of Fe^{2+} and its associated effects on the
72 thermal EoS of the magnesite-siderite system have only been previously investigated at
73 high pressures and room temperature.

74 Spin transitions of ferric and ferrous iron and their associated effects have also been
75 reported to occur in other iron-bearing mantle minerals at high pressures, including
76 ferropericlase, perovskite, and post-perovskite (See Lin and Tsuchiya (2008) and Lin et al.
77 (2013) for recent reviews). In particular, the spin transition of iron has been observed to
78 affect a number of physical and chemical properties of ferropericlase including density,
79 incompressibility, sound velocities, and transport properties (Lin et al. 2005, 2006, 2007a;
80 Tsuchiya et al. 2006; Fei et al. 2007b; Speziale et al. 2007; Crowhurst et al. 2008;
81 Marquardt et al. 2009a, 2009b; Wentzcovitch et al. 2009; Wu et al. 2009; Komabayashi
82 et al. 2010; Mao et al. 2011). Recent theoretical and experimental studies also show that
83 the spin transition becomes a broad, continuous spin crossover at high P - T conditions
84 (Tsuchiya et al., 2006; Lin et al. 2007b; Wentzcovitch et al. 2009; Wu et al. 2009;
85 Komabayashi et al. 2010; Mao et al. 2011). Along a typical mantle geotherm (Brown and
86 Shankland, 1981), the spin crossover in ferropericlase is expected to occur approximately
87 between 1700 and 2700-km depth (e.g., Mao et al. 2011). Therefore, studying the spin
88 transition and its associated effects on thermal EoS parameters in the magnesite-siderite

Revision 1: Magnesiosiderite Diffraction at high P - T , AM, 7/15/2013

89 system at relevant P - T conditions of the Earth's mantle would help us understand the
90 nature of the spin crossover as well as the characteristics of this potential deep-carbon
91 host.

92 In the present work, we have carried out synchrotron X-ray diffraction measurements
93 on magnesiosiderite $[(\text{Mg}_{0.35}\text{Fe}_{0.65})\text{CO}_3]$ in an externally-heated diamond anvil cell
94 (EHDAC) or a laser-heated diamond anvil cell (LHDAC) at high P - T conditions in order
95 to understand its thermal EoS parameters across the spin crossover. We used the P - V - T
96 relations of magnesiosiderite to model the spin-crossover diagram up to 80 GPa and 1200
97 K and to derive thermal EoS parameters for HS, LS, and mixed-spin states, respectively.
98 The modeled spin-crossover diagram of magnesiosiderite shows that increasing
99 temperature broadens the width of the spin crossover toward higher pressures. These
100 results are applied to decipher the role of magnesiosiderite in the lower-mantle deep-
101 carbon storage.

102

103 **EXPERIMENTAL METHODS**

104 A natural single-crystal magnesiosiderite from Brazil was used as the starting
105 material, which has also been previously studied by Lin et al. (2012) using optical Raman
106 and synchrotron X-ray diffraction spectroscopies at high pressures and room temperature.
107 Briefly, electron microprobe and XRD analyses showed that the sample is chemically
108 homogeneously within the analytical uncertainties, and has a composition
109 $(\text{Mg}_{0.33}\text{Mn}_{0.02}\text{Fe}_{0.65})\text{CO}_3$ with lattice parameters $a = 4.6753 (\pm 0.0012) \text{ \AA}$ and $c = 15.2794$
110 $(\pm 0.0030) \text{ \AA}$; for simplicity, the composition of the sample is referred to as

5

Revision 1: Magnesiosiderite Diffraction at high P - T , AM, 7/15/2013

111 $(\text{Mg}_{0.35}\text{Fe}_{0.65})\text{CO}_3$ by ignoring the manganese content and by keeping the amount of iron
112 fixed. Visual observations using a high-magnification optical microscope showed that the
113 single-crystal sample was optically homogenous without any signs of chemical inclusions
114 or variations in color. High P - T X-ray diffraction experiments were conducted at 13IDD
115 beamline of the GSECARS of the Advanced Photon Source (APS), Argonne National
116 Laboratory (ANL), using a monochromatic X-ray beam with a wavelength of 0.3344 Å.
117 Single-crystal or powder X-ray diffraction (XRD) measurements were performed using
118 an EHDAC (Kantor et al. 2012) or an LHDAC (Prakapenka et al. 2008). A MarCCD
119 detector was used to collect two-dimensional XRD images which were processed and
120 integrated using Fit2D software (Hammersley et al. 1996). The tilting and rotation of the
121 MarCCD detector relative to the incident X-ray beam were calibrated using cesium
122 dioxide (CeO_2) powder as the X-ray diffraction standard. The sample-detector distance
123 was calculated from the powder CeO_2 diffraction pattern at ambient conditions.

124 For the EHDAC experiments, both powder and single-crystal XRD measurements
125 were performed using Ne as the pressure medium. For the single-crystal experiments, a
126 piece of the single-crystal magnesiosiderite was cleaved from the natural crystal along
127 (101) plane and loaded into an EHDAC, together with a 5 μm pellet of Au powder as the
128 pressure calibrant (Fei et al. 2007a). A K-type thermocouple was attached to the pavilion
129 of the diamond, approximately 500 μm away from its culet, and used to monitor the
130 temperature. For the powder runs, powdered magnesiosiderite was mixed with 3 wt%
131 micro-sized Au powder as the pressure calibrant (Fei et al. 2007a) by mechanically
132 grinding the mixture for approximately 4 hours. Subsequently, the mixture was slightly
133 pressed between two opposing diamond anvils to form an approximately 15 μm thick

Revision 1: Magnesiosiderite Diffraction at high P - T , AM, 7/15/2013

134 disk. The powder sample disk was loaded into an EHDAC with 300 μm culets and a Re
135 gasket, which was pre-indented to 30 μm thick and had a drill hole of 150 μm diameter.

136 Two runs of the LHDAC experiments were conducted using the double-sided
137 Nd:YLF laser heating system at GSECARS (Prakapenka et al. 2008). The
138 aforementioned powder sample disk was sandwiched between two dried NaCl disks,
139 which functioned as the thermal insulator and pressure medium, in a symmetric DAC
140 with 300 or 200 μm culets and a Re gasket. To remove any potential air and moisture
141 contamination in the sample chamber, the sandwiched sample assemblage was evacuated
142 for 30 minutes before closing the sample chamber in vacuum using the high-pressure gas
143 loading system in the Mineral Physics Laboratory of the University of Texas at Austin.
144 Two infrared laser beams were focused down to 25 μm diameter on both sides of the
145 sample, and were co-axially aligned with the incoming X-ray beam using the X-ray
146 induced luminescence on the sample and NaCl (Prakapenka et al. 2008). Temperatures of
147 the heated samples were determined by fitting the measured thermal radiation spectra
148 assuming the Graybody approximation (Prakapenka et al. 2008). The uncertainty of
149 temperatures (1σ) was ± 50 K based on multiple temperature measurements from both
150 sides of the laser-heated sample. Pressures were calculated from *in situ* XRD patterns of
151 the Au standard (Fei et al. 2007a).

152

153 **RESULTS AND DATA ANALYSES**

154 XRD patterns of the sample were collected at five given temperatures (300 K, 450 K,
155 600 K, 750 K and 1200 K) in 1-3 GPa intervals up to 78 GPa (Figs. 1 and 2); data at 1200

7

Revision 1: Magnesiosiderite Diffraction at high P - T , AM, 7/15/2013

156 K were taken from the LHDAC experiments while all other high-temperature points were
157 obtained from the EHDAC experiments. We limited the laser heating temperature to
158 1200 K because Fe-rich magnesiosiderite has been reported to transform into a new
159 Fe^(III)-bearing high-pressure phase at temperatures above 1850 K and high pressures
160 (Boulard et al. 2011, 2012). The unit-cell parameters of the magnesiosiderite and Au in
161 this study were calculated using 3-8 diffraction lines, respectively, at high P - T (Fig. 3).
162 Analyses of the XRD patterns from heated and quenched sample assemblages only
163 showed diffraction peaks from the sample, Au calibrant, and Ne or NaCl medium,
164 indicating that the sample remained stable in the rhombohedral structure and that no
165 dissociation or chemical reaction had occurred in the sample during high P - T experiments
166 (Figs. 1 and 2). All error bars reported here are derived from standard error propagations
167 and represent $\pm 1\sigma$.

168 The compression curve of (Mg_{0.35}Fe_{0.65})CO₃ at 300 K shows a dramatic volume
169 reduction of 6.5% over a pressure interval of ~ 4 GPa from 43.4 (± 0.4) GPa to 47.5 (± 0.5)
170 GPa, consistent with the spin transition pressure reported previously (Mattila et al. 2007;
171 Shi et al. 2008; Lavina et al. 2009, 2010a, 2010b; Nagai et al. 2010; Farfan et al. 2012;
172 Lin et al. 2012). The P - V curves at given high temperatures clearly show an increase in
173 the onset pressure and the width of the volume reduction; i.e., the volume reduction at
174 1200 K starts at 53.2 (± 0.5) GPa and ends at 63 (± 0.5) GPa over a pressure interval of
175 approximately 10 GPa (Fig. 3). The P - V - T curves were used to derive thermal EoS
176 parameters of the HS, LS, and mixed-spin states as well as the spin-crossover diagram of
177 the magnesiosiderite.

178

Revision 1: Magnesiosiderite Diffraction at high P - T , AM, 7/15/2013

179 **Equation of state at room temperature**

180 The P - V curve of the sample at 300 K up to 40 GPa (before the abnormal volume
181 reduction) was fitted to a third-order Birch-Murnaghan EoS (BM EoS) to derive the unit-
182 cell volume (V_0), the bulk modulus (K_0) and the pressure derivative of the bulk modulus
183 (K'_0) at ambient conditions using the EosFit v5.2 programs (Birch 1978; Angel 2000),
184 yielding $V_0 = 289.2 (\pm 0.1) \text{ \AA}^3$, $K_0 = 109.2 (\pm 1.3) \text{ GPa}$, and $K'_0 = 4.9 (\pm 0.2)$ for the HS
185 state (Table 1). In order to identify the onset pressure for the occurrence of the LS state
186 (P_{LS}) and the ending pressure for the HS state (P_{HS}), our experimental data were
187 compared with the modeled P - V curve for the HS state (Speziale et al. 2007; Mao et al.
188 2011)—the P_{LS} and P_{HS} can thus be determined from the variation in the volume
189 difference between the experimental P - V data and the modeled HS P - V curve (Fig. 3
190 insert), yielding $P_{\text{LS}} = 43.4 (\pm 0.4) \text{ GPa}$ and $P_{\text{HS}} = 47.5 (\pm 0.5) \text{ GPa}$, with a width of 4.1
191 (± 0.9) GPa. Additionally, EoS parameters for the LS magnesiosiderite were obtained
192 from fitting the P - V data between 47.5 GPa and 78 GPa with the third order BM EoS
193 (Table 2). The derived V_0 , K_0 , and K'_0 values for the HS and LS states at 300 K are in
194 good agreement with previous reports (Lavina et al. 2009, 2010a, 2010b; Nagai et al.
195 2010; Farfan et al. 2012; Lin et al. 2012).

196

197 **Thermal equation of state parameters**

198 For P - V data at elevated temperatures, the third-order isothermal BM EoS was
199 employed to derive the thermal EoS parameters for the HS and LS states using the EosFit
200 v5.2 programs (Birch 1978; Angel 2000):

Revision 1: Magnesiosiderite Diffraction at high P - T , AM, 7/15/2013

$$201 \quad P(V, T) = \frac{3K_{0T}}{2} \left[\left(\frac{V_{0T}}{V} \right)^{\frac{7}{3}} - \left(\frac{V_{0T}}{V} \right)^{\frac{5}{3}} \right] \left\{ 1 + \frac{3}{4} (K'_{0T} - 4) \left[\left(\frac{V_{0T}}{V} \right)^{\frac{7}{3}} - 1 \right] \right\}$$

202 where $0T$ denotes ambient pressure and a given high temperature, respectively.
203 Neglecting higher-order pressure derivatives of the bulk modulus and assuming that K'_{0T}
204 is a constant in the temperature range of our study (Zhang et al. 1998), the K_{0T} can be
205 determined using the following equation:

$$206 \quad K_{0T} = K_0 + (\partial K_T / \partial T)_{0P} (T - 300)$$

207 where $(\partial K_T / \partial T)_{0P}$ is the temperature derivative of the bulk modulus at ambient pressure.
208 The $(\partial K_T / \partial T)_{0P}$ is found to be a constant within the temperature range of our study. The
209 zero-pressure unit-cell volume (V_{0T}) at an elevated temperature T is expressed as:

$$210 \quad V_{0T} = V_0 \exp \int_{300}^T \alpha_T dT$$

211 where α_T is the thermal expansion coefficient at high temperature and ambient pressure.
212 In our model here, α_T is assumed to be a linear function of temperature:

$$213 \quad \alpha_T = \alpha_0 + \alpha_1 T$$

214 where α_1 and α_2 are constants. We have also modeled the thermal expansion coefficient
215 using a polynomial function, instead of the above linear function, but the second-order
216 constant is found to be too insignificant to justify the use of the polynomial function
217 within our limited temperature range.

Revision 1: Magnesiosiderite Diffraction at high P - T , AM, 7/15/2013

218 The modeled P - V - T curves for the HS state were then used as the reference for
219 derivation of the P_{LS} and P_{HS} using the variation in the volume difference between the
220 modeled results and experimental data at high P - T (Fig. 3 insert). Thermal EoS
221 parameters of the LS state can then be determined using the same aforementioned
222 procedure. These analyses show that the HS state exhibits $(\partial K_T/\partial T)_{0P} = -0.0262$
223 (± 0.0021) GPa/K and α (K^{-1}) = $2.79 (\pm 0.21) \times 10^{-5} + 0.95 (\pm 0.30) \times 10^{-8} T$ (Table 1),
224 while the LS state has $(\partial K_T/\partial T)_{0P} = -0.0234 (\pm 0.0052)$ GPa/K and α (K^{-1}) = $2.31 (\pm 0.20)$
225 $\times 10^{-5} + 0.14 (\pm 0.09) \times 10^{-8} T$ (Table 2).

226

227 **Spin-crossover diagram**

228 The P - V - T relations of the magnesiosiderite were used to derive the fraction of the HS
229 and LS states for constructing the spin-crossover diagram. Following the thermodynamic
230 methods described previously (Tsuchiya et al. 2006; Speziale et al. 2007; Wentzcovitch
231 et al. 2009; Mao et al. 2011), the unit cell volume of the sample within the spin crossover
232 was treated as an ideal solid-solution mixture of the HS and LS states:

233
$$V = n_{LS}V_{LS} + (1 - n_{LS})V_{HS}$$

234 where V_{HS} and V_{LS} are the unit cell volume of the HS and LS states, respectively, and n_{LS}
235 is the LS fraction. With the experimentally-determined n_{LS} at a given temperature (Fig. 4),
236 the LS fraction of the magnesiosiderite at a given P - T condition was modeled using the
237 Gibbs free energy difference between the LS and HS states (ΔG_{LS-HS}) across the spin
238 crossover (Tsuchiya et al. 2006; Speziale et al. 2007; Wentzcovitch et al. 2009):

Revision 1: Magnesiosiderite Diffraction at high P - T , AM, 7/15/2013

239
$$n_{LS} = 1 / (1 + \exp(\Delta G_{LS-HS} / T)).$$

240 Here the P - T dependence of the ΔG_{LS-HS} is expressed using the following empirical
241 relation:

242
$$\Delta G_{LS-HS} = b_0 + b_1(P - P_{HS}) / (P_{LS} - P_{HS})$$

243 where b_0 and b_1 are two temperature-dependent constants, and P_{LS} and P_{HS} are the onset
244 pressure for the occurrence of the LS state and the ending pressure for the HS state,
245 respectively. Parameters b_0 and b_1 are derived from the non-linear least square fit of the
246 experimentally-determined n_{LS} as a function of P - T . We note that this model has been
247 successfully applied to derive the spin-crossover diagram of the lower-mantle
248 ferropericlase using experimentally-measured thermal P - V - T data (Mao et al. 2011).
249 Using the derived width of the spin transition and thermal EoS parameters of the
250 magnesiosiderite, the fraction of the LS state and the spin-crossover diagram can be
251 derived from modeling our data between 300 K and 1200 K at high pressures (Figs. 4 and
252 5). The spin-crossover diagram shows apparently positive values for the effective dP/dT
253 of the transition boundaries and the width of the spin crossover widens at higher
254 temperatures (Fig. 5).

255

256 **Thermal elastic properties along an isotherm**

257 Using the obtained thermal EoS parameters and the LS fraction, thermoelastic
258 properties of the magnesiosiderite, including thermal expansion coefficient (α),

Revision 1: Magnesiosiderite Diffraction at high P - T , AM, 7/15/2013

259 isothermal bulk modulus (K_T), and bulk sound velocity (V_Φ), have also been derived at
260 given temperatures (300 K, 450 K, 600 K, 750 K and 1200 K) and high pressures up to
261 80 GPa across the spin crossover (Figs. 6 and 7). The thermal expansion coefficient
262 across the transition is defined as (Mao et al. 2011):

$$263 \quad \alpha = \frac{1}{V} \frac{\partial V}{\partial T} = \frac{1}{V} \frac{\partial [n_{LS} V_{LS} + (1 - n_{LS}) V_{HS}]}{\partial T}.$$

264 The isothermal bulk modulus is calculated using the equation (Wentzcovitch et al. 2009):

$$265 \quad \frac{V}{K_T} = n_{LS} \frac{V_{LS}}{K_{LS}} + (1 - n_{LS}) \frac{V_{HS}}{K_{HS}} - (V_{LS} - V_{HS}) \left(\frac{\partial n_{LS}}{\partial P} \right)_T$$

266 where K_{HS} and K_{LS} are the isothermal bulk modulus of the HS and LS state at a given P - T
267 condition, respectively. The last term accounts for the pressure-dependent LS fraction
268 that can affect the modulus as a result of the anomalous volume reduction ($V_{LS} - V_{HS}$)
269 across the transition (Fig. 6(b)) (Wentzcovitch et al. 2009). With the derived K_T and α ,
270 the bulk sound velocity (V_Φ) can be calculated using the equations:

$$271 \quad V_\Phi = \sqrt{K_S / \rho}$$

$$272 \quad K_S = (1 + \alpha \gamma T) K_T$$

273 where K_S is the adiabatic bulk modulus, ρ is density, and γ is the thermodynamic
274 Grüneisen parameter. Because the γ value of the sample at high P - T remains unknown
275 across the spin transition, we used the following equation to calculate the γ value at
276 ambient conditions and assume it remains a constant at high P - T :

Revision 1: Magnesiosiderite Diffraction at high P - T , AM, 7/15/2013

277
$$\gamma = \frac{\alpha K_S}{\rho C_P}$$

278 where K_S is the adiabatic bulk modulus and C_P is the heat capacity at constant pressure.

279 Using the values of $\alpha = 3.08 \times 10^{-5} \text{ K}^{-1}$ (this study), $K_S = 113.4 \text{ GPa}$ (Sanchez-Valle et al.

280 2011), $\rho = 3.654 \text{ g/cm}^3$ (this study), and $C_P = 82.44 \text{ J/(mol}\cdot\text{K)}$ (Robie et al. 1984) at 300

281 K, the calculated γ value is $1.16 (\pm 0.12)$.

282

283 **DISCUSSIONS and IMPLICATIONS**

284 **Spin crossover at high P - T**

285 The modeled spin-crossover diagram of the magnesiosiderite shows an extended
286 crossover behavior at high temperatures with an apparently positive value for the
287 effective dP/dT of approximately 10 MPa/K (Fig. 5). Specifically, the width of the
288 transition is approximately 4 GPa at 300 K but expands to approximately 10 GPa at 1200
289 K. The onset pressure for the occurrence of the LS state increases from $43.4 (\pm 0.4) \text{ GPa}$
290 at 300 K to $53.2 (\pm 0.5) \text{ GPa}$ at 1200 K (Fig. 8). Such spin-crossover behavior has been
291 previously reported to occur in ferropicrlase theoretically and experimentally (Tsuchiya
292 et al., 2006; Lin et al. 2007b; Wentzcovitch et al. 2009; Wu et al. 2009; Komabayashi et
293 al. 2010; Mao et al. 2011). Compared with ferropicrlase, the spin crossover in
294 magnesiosiderite remains much narrower and occurs at relative lower pressures (Figs. 5
295 and 8). The relatively sharp spin crossover in the MgCO_3 - FeCO_3 system is likely a result
296 of the localized FeO_6 octahedra that are more isolated and separated from other iron ions

Revision 1: Magnesiosiderite Diffraction at high P - T , AM, 7/15/2013

297 in the surrounding FeO_6 octahedra (Lavina et al. 2010b). Previous theoretical and
298 experimental studies on ferropericlase $[(\text{MgFe})\text{O}]$ (e.g., Wentzcovitch et al. 2009; Mao et
299 al. 2011) have reported apparently positive values for the effective dP/dT slope. At a
300 given temperature, the spin transition is reported to be a pressure-induced volume-driven
301 transition in which the pressure-induced volume reduction increases the crystal-field
302 splitting energy that eventually overcomes the spin-pairing energy (e.g., Burns 1993;
303 Persson et al. 2006).

304 We note that the presence of nonhydrostaticity and pressure gradient in the sample
305 chamber may cause a broadening in the width of the spin crossover (Lin and Tsuchiya,
306 2008). In this study, the use of Ne pressure medium and the tightly focused X-ray beam
307 of less than 5 μm in diameter (FWHM) would minimize the influence of these factors.
308 Therefore, the broadening of the spin crossover at higher P - T can be treated as the
309 intrinsic phenomenon of the Fe^{2+} ions in magnesiosiderite at elevated temperatures, in
310 which high temperature provides higher configuration entropy to stabilize the mixture of
311 the HS and LS states (Burns 1993; Tsuchiya et al. 2006). Previous studies have shown
312 that the HS state is favored at higher temperatures due to the larger entropy for Fe^{2+} in the
313 octahedral site via the thermal expansion effect (Li 2007; Wentzcovitch et al. 2009).
314 Consequently, additional compression (smaller unit cell volume) is necessary for the LS
315 state to become stable at elevated temperatures.

316

317 **Compositional effects on the spin transition pressure**

Revision 1: Magnesiosiderite Diffraction at high P - T , AM, 7/15/2013

318 To illustrate the compositional effect on the transition pressure and thermal EoS
319 parameters in the MgCO_3 - FeCO_3 system as well as MgO - FeO system, we have plotted
320 our results and literature transition pressures (Fig. 9) for comparison (Badro et al. 2003;
321 Speziale et al. 2005; Lin et al. 2005, 2006, 2007b; Keppler et al. 2007; Fei et al. 2007b;
322 Crowhurst et al. 2008; Lavina et al. 2009, 2010a, 2010b; Komabayashi et al. 2010; Nagai
323 et al. 2010; Mao et al. 2011; Farfan et al. 2012; Lin et al. 2012). Among all iron-bearing
324 earth minerals, we note that the spin transitions in these two systems have been most
325 extensively documented using high-pressure X-ray and laser optical spectroscopic
326 techniques. The transition in the MgCO_3 - FeCO_3 system occurs at 45 (± 5) GPa without
327 observable compositional effects (Mattila et al. 2007; Shi et al. 2008; Lavina et al. 2009,
328 2010a, 2010b; Nagai et al. 2010; Farfan et al. 2012; Lin et al. 2012). That is, the
329 substitution of Fe^{2+} ions for Mg^{2+} ions in MgCO_3 does not show any appreciable effect on
330 the spin transition pressure. This can be used to support the solid-solution model that we
331 used to derive the spin fraction as a function of the volume reduction. In the $(\text{MgFe})\text{O}$
332 system, on the other hand, the transition pressure generally increases from 40-50 GPa for
333 MgO -rich part (ferropericlase) to approximately 102 GPa for FeO -rich part
334 (magnesiowustite) (Badro et al. 2003; Speziale et al. 2005; Lin et al. 2005, 2006, 2007b;
335 Persson et al. 2006; Keppler et al. 2007; Fei et al. 2007b; Crowhurst et al. 2008;
336 Komabayashi et al. 2010; Mao et al. 2011), indicating a strong compositional effect that
337 stabilizes the high-spin state. These analyses indicate that the Fe^{2+} - Fe^{2+} exchange
338 interaction in the $(\text{MgFe})\text{O}$ system plays a more significant role in the spin transition than
339 that in the $(\text{MgFe})\text{CO}_3$ system (Figs. 8 and 9) (Lin et al. 2006).

340

Revision 1: Magnesiosiderite Diffraction at high P - T , AM, 7/15/2013

341 **Abnormal thermal EoS and stability of $(\text{MgFe})\text{CO}_3$**

342 Previous studies on the EoS of $(\text{MgFe})\text{CO}_3$ have shown that the spin transition of iron
343 causes approximately 6-10% volume reduction from the HS state to the LS state in
344 magnesiosiderite containing more than 65% iron (Lavina et al. 2009, 2010b; Nagai et al.
345 2010; Farfan et al. 2012; Lin et al. 2012). However, thermal EoS parameters within the
346 spin transition remain unclear at high P - T . Our thermoelastic modeling of the P - V - T
347 relations of the magnesiosiderite shows abnormal behavior in the thermal expansion
348 coefficient, isothermal bulk modulus, and bulk sound velocity within the spin transition
349 (Figs. 6 and 7). Specifically, within the transition, the thermal expansion coefficient
350 increases by approximately a factor of forty at 300 K and twenty at 1200 K, whereas the
351 isothermal bulk modulus and the bulk sound velocity decrease by approximately 75% and
352 50% at 1200 K, respectively. It should be noted that such abnormal behaviors within the
353 spin transitions have been reported for the lower-mantle ferropericlase (Speziale et al.
354 2007; Crowhurst et al. 2008; Wentzcovitch et al. 2009; Wu et al. 2009; Mao et al. 2011).
355 In comparison to the lower-mantle ferropericlase, our magnesiosiderite sample exhibits
356 similar abnormal behaviors across the spin transition, although the magnitude of the
357 changes was much higher than that of ferropericlase as a result of the larger volume
358 reduction across the sharper spin transition at high P - T .

359 The spin transition increases the isothermal bulk modulus by approximately 10% and
360 decreases the thermal expansion coefficient by nearly 20%, making the LS state much
361 more incompressible and less expandable than the HS state. The effects of the spin
362 transition on the bulk modulus can be understood in terms of the relative ionic radii of the
363 HS-LS Fe^{2+} and Mg^{2+} cations in the system which has been investigated and

Revision 1: Magnesiosiderite Diffraction at high P - T , AM, 7/15/2013

364 systematically tabulated in previous studies (Shannon and Prewitt 1969; Shannon 1976;
365 Hazen and Finger 1982). Previous studies have shown that in the octahedral coordination
366 the effective ionic radius of the HS Fe^{2+} is 0.78 Å and the Mg^{2+} ion is 0.72 Å (Shannon
367 and Prewitt 1969; Shannon 1976), indicating that the substitution of Fe^{2+} for Mg^{2+} would
368 yield a larger unit cell volume in the $(\text{MgFe})\text{CO}_3$ system, i.e., the unit cell volume of the
369 magnesiosiderite $[(\text{Mg}_{0.35}\text{Fe}_{0.65})\text{CO}_3]$ is 289.2 Å³ while magnesite (MgCO_3) is 279.3 Å³
370 (Zhang et al. 1997; Fiquet et al. 2002; Litasov et al. 2008). On the other hand, the
371 extrapolated unit cell volume of the LS magnesiosiderite of 265.1 Å³ at ambient
372 conditions is much smaller than the HS state counterpart, suggesting that the LS state is
373 intrinsically more incompressible than the HS state, confirming the previously reported
374 empirical relationship between the atomic compressibility and the ionic radii (Hazen and
375 Finger 1982). As a result of the volume collapse, the LS magnesiosiderite also exhibits a
376 smaller unit cell volume than the end-member magnesite at given P - T conditions,
377 showing that the effective ionic radius of the LS Fe^{2+} is thus smaller than the Mg^{2+} ion
378 (Fig. 10) (e.g., Shannon and Prewitt 1969; Hazen and Finger 1982; Lavina et al. 2009).

379 To understand the stability of the magnesiosiderite at high P - T conditions, we have
380 derived its volume and density differences from the MgCO_3 reference (Figs. 10 and 11).
381 For the HS state, this volume difference is nearly 4% at 300 K and 3% at 1200 K before
382 the spin transition. The volume difference decreases dramatically to about -2% for the LS
383 state between 300 K and 1200 K; that is, the LS state has a much lower volume than the
384 end member MgCO_3 counterpart. This volume difference in the LS state remains almost
385 constant as a function of pressure, revealing that the LS state has similar
386 incompressibility with the end member MgCO_3 .

Revision 1: Magnesiosiderite Diffraction at high P - T , AM, 7/15/2013

387 Recent high P - T experimental and theoretical studies have reported that magnesite
388 remains stable in the calcite structure (space group $R\bar{3}c$) at relevant P - T conditions of the
389 lower mantle, instead of undergoing a dissociation that releases carbon dioxide into the
390 surrounding mantle materials (Isshiki et al. 2004; Skorodumova et al. 2005; Oganov et al.
391 2008). Since the lower-mantle magnesite likely incorporates approximately 20% iron and
392 the low-spin ferromagnesite has a smaller unit cell volume than the high-spin counterpart,
393 it is conceivable that the low-spin ferromagnesite can become the major deep-carbon host
394 mineral in the lower part of the lower mantle. Specifically, extrapolations of our results
395 show that low-spin ferromagnesite containing 20 mole% iron would be 0.6% smaller in
396 volume and 7% denser than the end-member magnesite at relevant P - T conditions of the
397 subducted slabs. The relatively dense low-spin ferromagnesite likely becomes more
398 stable than the high-spin counterpart and can promote partitioning of iron into the LS
399 state making it an even denser and much more stable phase in the lower-mantle
400 conditions (Badro et al. 2005; Irifune et al. 2010). Detailed knowledge of the
401 thermodynamic parameters of the whole mineralogical assemblage of the lower mantle
402 will be needed in order to fully explore the thermodynamic stability of the ferromagnesite
403 in different spin states. Future studies of physical and chemical properties of the low-spin
404 ferromagnesite with surrounding mineral assemblages such as ferropericlase and silicate
405 perovskite at relevant P - T conditions are still needed to understand the geophysical and
406 geochemical consequences of the spin crossover in the lower mantle.

407

Revision 1: Magnesiosiderite Diffraction at high P - T , AM, 7/15/2013

408 **ACKNOWLEDGEMENTS**

409 J. F. Lin acknowledges supports from the US National Science Foundation (EAR-
410 1053446 and EAR-1056670), Energy Frontier Research Centers (EFree), and the
411 Carnegie/DOE Alliance Center (CDAC). Synchrotron works of the study were performed
412 at HPCAT of the APS, ANL. HPCAT is supported by CIW, CDAC, UNLV and LLNL
413 through funding from DOE-NNSA, DOE-BES and NSF. APS is supported by DOE-BES,
414 under Contract No. DE-AC02-06CH11357. The authors also thank J. Wu, D. Fan, J.
415 Yang, and B. Chen for constructive discussions.

416

Revision 1: Magnesiosiderite Diffraction at high P - T , AM, 7/15/2013

417 **Figure Captions**

418 **Figure 1.** Representative X-ray diffraction patterns of magnesiosiderite
419 $[(\text{Mg}_{0.35}\text{Fe}_{0.65})\text{CO}_3]$ measured from an EHDAC. Gold (Au) was used as the internal
420 pressure calibrant (Fei et al. 2007a), while Neon (Ne) was used as the thermal insulator
421 and pressure medium. The wavelength of the monochromatic X-ray beam was 0.3344 Å.

422 **Figure 2.** Representative X-ray diffraction patterns of magnesiosiderite
423 $[(\text{Mg}_{0.35}\text{Fe}_{0.65})\text{CO}_3]$ at high pressures and 1200 K measured from a LHDAC. HS and LS
424 states are labeled to illustrate the splitting of the diffraction peaks across the spin
425 transition. Gold (Au) was used as the internal pressure calibrant (Fei et al. 2007a), while
426 sodium chloride (NaCl) in B1 or B2 structure was used as the thermal insulator and
427 pressure medium. The wavelength of the monochromatic X-ray beam was 0.3344 Å.

428 **Figure 3.** Pressure-volume relations of magnesiosiderite $[(\text{Mg}_{0.35}\text{Fe}_{0.65})\text{CO}_3]$ at high
429 P - T . Open circles: experimental measurements; lines: modeled results. The insert figure
430 shows the volume difference between experimental results and the HS state reference.

431 **Figure 4.** Low-spin fraction of magnesiosiderite $[(\text{Mg}_{0.35}\text{Fe}_{0.65})\text{CO}_3]$ as a function of
432 pressure compared with the fitting results. Open circles: experimental measurements;
433 lines: fitting results. Vertical ticks represent the error for the low-spin fraction. Errors are
434 calculated using standard error propagations from our modeled parameters.

435 **Figure 5.** Spin crossover of iron in magnesiosiderite $[(\text{Mg}_{0.35}\text{Fe}_{0.65})\text{CO}_3]$ at high P - T .
436 The color bar on the right represents the fraction of the LS state.

Revision 1: Magnesiosiderite Diffraction at high P - T , AM, 7/15/2013

437 **Figure 6.** Thermal elastic parameters of magnesiosiderite $[(\text{Mg}_{0.35}\text{Fe}_{0.65})\text{CO}_3]$ at
438 constant temperatures. α : thermal expansion coefficient; K_T : isothermal bulk modulus; V_Φ :
439 bulk sound velocity. Vertical ticks: representative errors ($\pm 1\sigma$) for α , K_T and V_Φ ,
440 respectively.

441 **Figure 7.** Variations of thermal elastic parameters for the LS magnesiosiderite at
442 constant temperatures using the HS state as the reference. α : thermal expansion
443 coefficient; K_T : isothermal bulk modulus; V_Φ : bulk sound velocity. Vertical ticks:
444 representative errors.

445 **Figure 8.** Comparison of the low-spin fraction between magnesiosiderite and
446 ferropicriase at high P - T . Solid lines: magnesiosiderite; dashed lines: ferropicriase
447 $[(\text{Mg}_{0.75}\text{Fe}_{0.25})\text{O}; \text{fp}25]$ (Mao et al. 2011).

448 **Figure 9.** Comparison of the spin transition pressures in $(\text{MgFe})\text{CO}_3$ and $(\text{MgFe})\text{O}$
449 solid solution systems. Solid diamonds: $(\text{MgFe})\text{CO}_3$ (Lavina et al. 2009, 2010a, 2010b;
450 Nagai et al. 2010; Farfan et al. 2012; Lin et al. 2012); open circles: $(\text{MgFe})\text{O}$ (Badro et al.
451 2003; Speziale et al. 2005; Lin et al. 2005, 2006, 2007b; Keppler et al. 2007; Fei et al.
452 2007b; Crowhurst et al. 2008; Komabayashi et al. 2010; Mao et al. 2011).

453 **Figure 10.** Comparison of the thermal pressure-volume relations (a) and volume
454 differences (b) between magnesiosiderite and magnesite (MgCO_3) at high P - T . (a) Solid
455 lines: the fitted thermal P - V curves of magnesiosiderite; dashed lines: the fitted thermal
456 P - V curves of magnesite (Zhang et al. 1997; Litasov et al. 2008). Solid lines in (b) show

Revision 1: Magnesiosiderite Diffraction at high P - T , AM, 7/15/2013

457 the volume differences across the spin transition using magnesite (V_{MgCO_3}) as the
458 reference. Vertical ticks: representative errors.

459 **Figure 11.** Comparison of the thermal pressure-density relations and density
460 differences between magnesiosiderite and magnesite (MgCO_3) at high P - T . (a) Solid lines:
461 fitted thermal P - ρ curves of magnesiosiderite; dashed lines: fitted thermal P - ρ curves of
462 magnesite (Zhang et al. 1997; Litasov et al. 2008). Solid lines in (b) show the density
463 differences across the spin transition using the HS magnesiosiderite as the reference;
464 Solid lines in (c) show the density differences across the spin transition using magnesite
465 (ρ_{MgCO_3}) as the reference. Vertical ticks: representative errors.

Revision 1: Magnesiosiderite Diffraction at high P - T , AM, 7/15/2013

466 **REFERENCES CITED**

467 Alt, J.C., and Teagle, D.A.H. (1999) The uptake of carbon during alteration of ocean
468 crust. *Geochimica et Cosmochimica Acta*, 63(10), 1527-1535.

469 Angel, R.J. (2000) Equations of State. *Reviews in Mineralogy and Geochemistry*, 41(1),
470 35-59.

471 Badro, J., Fiquet, G., and Guyot, F. (2005) Thermochemical state of the lower mantle:
472 New insights from mineral physics. *Earth's Deep Mantle: Structure, Composition, and*
473 *Evolution*, 160, p. 241-260. AGU, Washington, DC.

474 Badro, J., Fiquet, G., Guyot, F., Rueff, J.-P., Struzhkin, V.V., Vankó, G., and Monaco, G.
475 (2003) Iron Partitioning in Earth's Mantle: Toward a Deep Lower Mantle
476 Discontinuity. *Science*, 300(5620), 789-791.

477 Berg, G.W. (1986) Evidence for carbonate in the mantle. *Nature*, 324(6092), 50-51.

478 Birch, F. (1978) Finite strain isotherm and velocities for single-crystal and polycrystalline
479 NaCl at high pressures and 300 K. *Journal of Geophysical Research: Solid Earth*,
480 83(B3), 1257-1268.

481 Boulard, E., Gloter, A., Corgne, A., Antonangeli, D., Auzende, A., Perrillat, J., Guyot, F.,
482 and Fiquet, G. (2011) New host for carbon in the deep Earth. *Proceedings of the*
483 *National Academy of Sciences of the United States of America*, 108(13), 5184-7.

484 Boulard, E., Menguy, N., Auzende, A.L., Benzerara, K., Bureau, H., Antonangeli, D.,
485 Corgne, A., Morard, G., Siebert, J., Perrillat, J.P., Guyot, F., and Fiquet, G. (2012)

Revision 1: Magnesiosiderite Diffraction at high *P-T*, AM, 7/15/2013

- 486 Experimental investigation of the stability of Fe-rich carbonates in the lower mantle. J.
487 Geophys. Res., 117(B2), B02208.
- 488 Brown, J.M., and Shankland, T.J. (1981) Thermodynamic parameters in the Earth as
489 determined from seismic profiles. Geophysical Journal of the Royal Astronomical
490 Society, 66(3), 579-596.
- 491 Burns, R.G. (1993) Mineralogical Applications of Crystal Field Theory. Cambridge
492 University Press, 2nd Ed.
- 493 Crowhurst, J.C., Brown, J.M., Goncharov, A.F., and Jacobsen, S.D. (2008) Elasticity of
494 (Mg,Fe)O Through the Spin Transition of Iron in the Lower Mantle. Science,
495 319(5862), 451-453.
- 496 Dasgupta, R., Chi, H., Shimizu, N., Buono, A.S., and Walker, D. (2013) Carbon solution
497 and partitioning between metallic and silicate melts in a shallow magma ocean:
498 Implications for the origin and distribution of terrestrial carbon. Geochimica et
499 Cosmochimica Acta, 102(2013), 191-212.
- 500 Dasgupta, R., and Hirschmann, M.M. (2010) The deep carbon cycle and melting in
501 Earth's interior. Earth and Planetary Science Letters, 298(1-2), 1-13.
- 502 Dasgupta, R., Hirschmann, M.M., and Withers, A.C. (2004) Deep global cycling of
503 carbon constrained by the solidus of anhydrous, carbonated eclogite under upper
504 mantle conditions. Earth and Planetary Science Letters, 227(1-2), 73-85.
- 505 Farfan, G., Wang, S., Ma, H., Caracas, R., and Mao, W.L. (2012) Bonding and structural
506 changes in siderite at high pressure. American Mineralogist, 97(8-9), 1421-1426.

Revision 1: Magnesiosiderite Diffraction at high *P-T*, AM, 7/15/2013

- 507 Fei, Y., Ricolleau, A., Frank, M., Mibe, K., Shen, G., and Prakapenka, V. (2007a)
508 Toward an internally consistent pressure scale. Proceedings of the National Academy
509 of Sciences of the United States of America, 104(22), 9182-9186.
- 510 Fei, Y., Zhang, L., Corgne, A., Watson, H., Ricolleau, A., Meng, Y., and Prakapenka, V.
511 (2007b) Spin transition and equations of state of (Mg, Fe)O solid solutions.
512 Geophysical Research Letters, 34(17), L17307.
- 513 Fiquet, G., Guyot, F., Kunz, M., Matas, J., Andrault, D., and Hanfland, M. (2002)
514 Structural refinements of magnesite at very high pressure. American Mineralogist,
515 87(8-9), 1261-1265.
- 516 Gaillard, F., Malki, M., Iacono-Marziano, G., Pichavant, M., and Scaillet, B. (2008)
517 Carbonatite Melts and Electrical Conductivity in the Asthenosphere. Science,
518 322(5906), 1363-1365.
- 519 Hammersley, A.P., Svensson, S.O., Hanfland, M., Fitch, A.N., and Hausermann, D.
520 (1996) Two-dimensional detector software: From real detector to idealised image or
521 two-theta scan. High Pressure Research, 14(4-6), 235-248.
- 522 Hazen, R.M., and Finger, L.W. (1982) Comparative crystal chemistry. A Wiley-
523 Interscience Publication, New York, pp. 165-193.
- 524 Hazen, R.M., Hemley, R.J., and Mangum, A.J. (2012) Carbon in Earth's interior: Storage,
525 cycling, and life. Eos, Transactions American Geophysical Union, 93(2), 17-18.

Revision 1: Magnesiosiderite Diffraction at high *P-T*, AM, 7/15/2013

- 526 Irifune, T., Shinmei, T., McCammon, C.A., Miyajima, N., Rubie, D.C., and Frost, D.J.
527 (2010) Iron partitioning and density changes of pyrolite in Earth's lower mantle.
528 Science, 327(5962), 193-195.
- 529 Isshiki, M., Irifune, T., Hirose, K., Ono, S., Ohishi, Y., Watanuki, T., Nishibori, E.,
530 Takata, M., and Sakata, M. (2004) Stability of magnesite and its high-pressure form
531 in the lowermost mantle. Nature, 427(6969), 60-63.
- 532 Kantor, I., Prakapenka, V., Kantor, A., Dera, P., Kurnosov, A., Sinogeikin, S.,
533 Dubrovinskaia, N., and Dubrovinsky, L. (2012) BX90: A new diamond anvil cell
534 design for X-ray diffraction and optical measurements. Review of Scientific
535 Instruments, 83(12), 125102-6.
- 536 Keppler, H., Kantor, I., and Dubrovinsky, L.S. (2007) Optical absorption spectra of
537 ferropericlase to 84 GPa. American Mineralogist, 92(2-3), 433-436.
- 538 Keppler, H., Wiedenbeck, M., and Shcheka, S.S. (2003) Carbon solubility in olivine and
539 the mode of carbon storage in the Earth's mantle. Nature, 424(6947), 414-6.
- 540 Komabayashi, T., Hirose, K., Nagaya, Y., Sugimura, E., and Ohishi, Y. (2010) High-
541 temperature compression of ferropericlase and the effect of temperature on iron spin
542 transition. Earth and Planetary Science Letters, 297(3-4), 691-699.
- 543 Lavina, B., Dera, P., Downs, R.T., Prakapenka, V., Rivers, M., Sutton, S., and Nicol, M.
544 (2009) Siderite at lower mantle conditions and the effects of the pressure-induced
545 spin-pairing transition. Geophysical Research Letters, 36(23), L23306.

Revision 1: Magnesiosiderite Diffraction at high *P-T*, AM, 7/15/2013

- 546 Lavina, B., Dera, P., Downs, R.T., Tschauner, O., Yang, W., Shebanova, O., and Shen, G.
547 (2010a) Effect of dilution on the spin pairing transition in rhombohedral carbonates.
548 High Pressure Research, 30(2), 224-229.
- 549 Lavina, B., Dera, P., Downs, R.T., Yang, W., Sinogeikin, S., Meng, Y., Shen, G., and
550 Schiferl, D. (2010b) Structure of siderite FeCO₃ to 56 GPa and hysteresis of its spin-
551 pairing transition. Physical Review B, 82(6), 064110.
- 552 Li, J. (2007) Electronic Transitions and Spin States in the Lower Mantle. In K. Hirose, J.
553 Brodholt, T. Lay, and D. Yuen, Eds. Post-Perovskite: The Last Mantle Phase
554 Transition, Geophysical Monograph Series 174, p. 47-68. American Geophysical
555 Union, Washington, D. C.
- 556 Lin, J.-F., Gavriluk, A.G., Struzhkin, V.V., Jacobsen, S.D., Sturhahn, W., Hu, M.Y.,
557 Chow, P., and Yoo, C.-S. (2006) Pressure-induced electronic spin transition of iron in
558 magnesiowustite-(Mg,Fe)O. Physical Review B, 73(11), 113107.
- 559 Lin, J.-F., Liu, J., Jacobs, C., and Prakapenka, V.B. (2012) Vibrational and elastic
560 properties of ferromagnesite across the electronic spin-pairing transition of iron.
561 American Mineralogist, 97(4), 583-591.
- 562 Lin, J.-F., Speziale, S., Mao, Z., and Marquardt, H. (2013) Effects of the electronic spin
563 transitions of iron in lower mantle minerals: Implications for deep mantle geophysics
564 and geochemistry. Reviews of Geophysics, 51, 2012RG000414.

Revision 1: Magnesiosiderite Diffraction at high P - T , AM, 7/15/2013

- 565 Lin, J.-F., Struzhkin, V.V., Jacobsen, S.D., Hu, M.Y., Chow, P., Kung, J., Liu, H., Mao,
566 H., and Hemley, R.J. (2005) Spin transition of iron in magnesiowüstite in the Earth's
567 lower mantle. *Nature*, 436(7049), 377-80.
- 568 Lin, J.-F., and Tsuchiya, T. (2008) Spin transition of iron in the Earth's lower mantle.
569 *Physics of the Earth and Planetary Interiors*, 170(3–4), 248-259.
- 570 Lin, J.-F., Vankó, G., Jacobsen, S.D., Iota, V., Struzhkin, V.V., Prakapenka, V.B.,
571 Kuznetsov, A., and Yoo, C. (2007b) Spin transition zone in Earth's lower mantle.
572 *Science*, 317(5845), 1740-3.
- 573 Lin, J.-F., Weir, S.T., Jackson, D.D., Evans, W.J., Vohra, Y.K., Qiu, W., and Yoo, C.-S.
574 (2007a) Electrical conductivity of the lower-mantle ferropericlase across the
575 electronic spin transition. *Geophysical Research Letters*, 34(16), L16305.
- 576 Litasov, K.D., Fei, Y., Ohtani, E., Kuribayashi, T., and Funakoshi, K. (2008) Thermal
577 equation of state of magnesite to 32 GPa and 2073 K. *Physics of the Earth and*
578 *Planetary Interiors*, 168(3–4), 191-203.
- 579 Mao, Z., Lin, J.-F., Liu, J., and Prakapenka, V.B. (2011) Thermal equation of state of
580 lower-mantle ferropericlase across the spin crossover. *Geophysical Research Letters*,
581 38(23), L23308.
- 582 Marquardt, H., Speziale, S., Reichmann, H.J., Frost, D.J., and Schilling, F.R. (2009a)
583 Single-crystal elasticity of $(\text{Mg}_{0.9}\text{Fe}_{0.1})\text{O}$ to 81 GPa. *Earth and Planetary Science*
584 *Letters*, 287(3–4), 345-352.

Revision 1: Magnesiosiderite Diffraction at high *P-T*, AM, 7/15/2013

- 585 Marquardt, H., Speziale, S., Reichmann, H.J., Frost, D.J., Schilling, F.R., and Garnero,
586 E.J. (2009b) Elastic shear anisotropy of ferropericlase in Earth's lower mantle.
587 Science, 324(5924), 224-6.
- 588 Mattila, A., Pylkkänen, T., Rueff, J.P., Huotari, S., Vankó, G., Hanfland, M., Lehtinen,
589 M., and Hämäläinen, K. (2007) Pressure induced magnetic transition in siderite
590 FeCO₃ studied by x-ray emission spectroscopy. Journal of Physics: Condensed Matter,
591 19(38), 386206.
- 592 Nagai, T., Ishido, T., Seto, Y., Nishio-Hamane, D., Sata, N., and Fujino, K. (2010)
593 Pressure-induced spin transition in FeCO₃-siderite studied by X-ray diffraction
594 measurements. Journal of Physics: Conference Series, 215(1), 012002.
- 595 Oganov, A.R., Ono, S., Ma, Y., Glass, C.W., and Garcia, A. (2008) Novel high-pressure
596 structures of MgCO₃, CaCO₃ and CO₂ and their role in Earth's lower mantle. Earth
597 and Planetary Science Letters, 273(1–2), 38-47.
- 598 Pal'yanov, Y.N., Sokol, A.G., Borzdov, Y.M., Khokhryakov, A.F., and Sobolev, N.V.
599 (1999) Diamond formation from mantle carbonate fluids. Nature, 400(6743), 417-418.
- 600 Persson, K., Bengtson, A., Ceder, G., and Morgan, D. (2006) Ab initio study of the
601 composition dependence of the pressure-induced spin transition in the (Mg_{1-x},Fe_x)O
602 system. Geophysical Research Letters, 33(16), L16306.
- 603 Prakapenka, V.B., Kubo, A., Kuznetsov, A., Laskin, A., Shkurikhin, O., Dera, P., Rivers,
604 M.L., and Sutton, S.R. (2008) Advanced flat top laser heating system for high

Revision 1: Magnesiosiderite Diffraction at high *P-T*, AM, 7/15/2013

- 605 pressure research at GSECARS: application to the melting behavior of germanium.
606 High Pressure Research, 28(3), 225-235.
- 607 Robie, R.A., Haselton, H.T., and Hemingway, B.S. (1984) Heat capacities and entropies
608 of rhodochrosite (MnCO_3) and siderite (FeCO_3) between 5 and 600 K. American
609 Mineralogist, 69(3-4), 349-357.
- 610 Sanchez-Valle, C., Ghosh, S., and Rosa, A.D. (2011) Sound velocities of ferromagnesian
611 carbonates and the seismic detection of carbonates in eclogites and the mantle.
612 Geophysical Research Letters, 38(24), L24315.
- 613 Shannon, R.D. (1976) Revised effective ionic radii and systematic studies of interatomic
614 distances in halides and chalcogenides. Acta Crystallographica Section A, 32(5), 751-
615 767.
- 616 Shannon, R.D., and Prewitt, C.T. (1969) Effective ionic radii in oxides and fluorides.
617 Acta Crystallographica Section B, 25(5), 925-946.
- 618 Shi, H., Luo, W., Johansson, B., and Ahuja, R. (2008) First-principles calculations of the
619 electronic structure and pressure-induced magnetic transition in siderite FeCO_3 .
620 Physical Review B, 78(15), 155119.
- 621 Skorodumova, N.V., Belonoshko, A.B., Huang, L., Ahuja, R., and Johansson, B. (2005)
622 Stability of the MgCO_3 structures under lower mantle conditions. American
623 Mineralogist, 90(5-6), 1008-1011.
- 624 Speziale, S., Lee, V.E., Clark, S.M., Lin, J.F., Pasternak, M.P., and Jeanloz, R. (2007)
625 Effects of Fe spin transition on the elasticity of $(\text{Mg,Fe})\text{O}$ magnesiowüstites and

Revision 1: Magnesiosiderite Diffraction at high *P-T*, AM, 7/15/2013

626 implications for the seismological properties of the Earth's lower mantle. Journal of
627 Geophysical Research: Solid Earth, 112, B10212.

628 Speziale, S., Milner, A., Lee, V.E., Clark, S.M., Pasternak, M.P., and Jeanloz, R. (2005)
629 Iron spin transition in Earth's mantle. Proceedings of the National Academy of
630 Sciences of the United States of America, 102(50), 17918-17922.

631 Tsuchiya, T., Wentzcovitch, R.M., da Silva, C.R.S., and de Gironcoli, S. (2006) Spin
632 Transition in Magnesiowüstite in Earth's Lower Mantle. Physical Review Letters,
633 96(19), 198501.

634 Wentzcovitch, R.M., Justo, J.F., Wu, Z., da Silva, C.R.S., Yuen, D.A., and Kohlstedt, D.
635 (2009) Anomalous compressibility of ferropericlase throughout the iron spin cross-
636 over. Proceedings of the National Academy of Sciences of the United States of
637 America, 106(21), 8447-8452.

638 Wu, Z., Justo, J.F., da Silva, C.R.S., de Gironcoli, S., and Wentzcovitch, R.M. (2009)
639 Anomalous thermodynamic properties in ferropericlase throughout its spin crossover.
640 Physical Review B, 80(1), 014409.

641 Zhang, J., Martinez, I., Guyot, F., Gillet, P., and Saxena, S.K. (1997) X-ray diffraction
642 study of magnesite at high pressure and high temperature. Physics and Chemistry of
643 Minerals, 24(2), 122-130.

644 Zhang, J., Martinez, I., Guyot, F., and Reeder, R.J. (1998) Effects of Mg-Fe²⁺ substitution
645 in calcite-structure carbonates; thermoelastic properties. American Mineralogist,
646 83(3-4), 280-287.

Revision 1: Magnesiosiderite Diffraction at high P - T , AM, 7/15/2013

647 **TABLE 1.** Thermal elastic parameters of the Fe-bearing magnesite [(MgFe)CO₃] in the
 648 high-spin state at ambient conditions. The thermal equation of state parameters were
 649 derived using the Birch-Murnaghan EOS when possible (Birch 1978). Literature values
 650 were refitted with the linear function for the thermal expansion coefficients in order to
 651 have more consistent systematic comparisons. Error bars represent one standard deviation
 652 in experimental uncertainties in our study.

	V_0 (Å ³)	K_{0T} (GPa)	K'_T	$(\partial K_T/\partial T)_{0P}$ (GPa/K)	α_0 (10 ⁻⁵ K ⁻¹)	α_1 (10 ⁻⁸ K ⁻²)
This study ^a	289.2 (±0.1)	109.2 (±1.3)	4.9 (±0.2)	-0.0262 (±0.0021)	2.79(±0.21)	0.95(±0.30)
Lin et al. (2012) ^a	289.1 (±0.1)	108 (±2)	4.8 (±0.2)			
Lavina et al. (2010b) ^b	294.4 (±0.3)	110 (±2)	4.6 (±0.2)			
Lavina et al. (2010a) ^c	281.0 (±0.5)	102.8 (±0.3)	5.44			
Nagai et al. (2010) ^d	293.5 (±0.1)	120 (±3)	4.3			
Zhang et al. (1998) ^e	292.828 (±0.035)	117 (±1)	4*	-0.031(±0.003)	1.76(±0.35)	3.46(±0.62)
Zhang et al. (1998) ^f	288.314 (±0.133)	112 (±1)	4*	-0.026(±0.002)	2.09(±0.23)	2.97(±0.39)
Litasov et al. (2008) ^g	279.55 (±0.02)	97.1 (±0.5)	5.44(±0.07)	-0.013(±0.001)	4.03(±0.07)	0.49(±0.10)
Isshiki et al. (2004) ^h		103 (±2)	5			
Fiquet et al. (2002) ⁱ	279.2 (±0.2)	108 (±3)	5.0 (±0.2)			
Zhang et al. (1997) ⁱ	279.32 (±0.15)	103 (±1)	4*	-0.021(±0.002)	3.15(±0.17)	2.32(±0.28)

^a (Fe_{0.65}Mg_{0.33}Mn_{0.02})CO₃; ^b (Fe_{0.96}Mg_{0.04})CO₃; ^c (Mg_{0.87}Fe_{0.12}Ca_{0.01})CO₃; ^d (Fe_{0.73}Mg_{0.22}Mn_{0.05})CO₃;

^e (Fe_{0.998}Mn_{0.002})CO₃; ^f (Fe_{0.60}Mg_{0.38}Mn_{0.02})CO₃; ^g (Mg_{0.975}Fe_{0.015}Mn_{0.006}Ca_{0.004})CO₃; ^h (Mg_{0.994}Ca_{0.006})CO₃; ⁱ MgCO₃.

*Fixed

653

654

Revision 1: Magnesiosiderite Diffraction at high P - T , AM, 7/15/2013

655 **TABLE 2.** Thermal elastic parameters of the low-spin magnesiosiderite. The thermal
656 equation of state parameters were derived using the Birch-Murnaghan EOS (Birch 1978).
657 Error bars represent one standard deviation in experimental uncertainties in our study.

	$V_0(\text{\AA}^3)$	$K_{0T}(\text{GPa})$	K'_T	$(\partial K_T/\partial T)_{0P}$ (GPa/K)	α_0 (10^{-5} K^{-1})	α_1 (10^{-8} K^{-2})
This study (LS) ^a	265.1 (± 3.2)	124.6 (± 3.3)	5.3 (± 0.2)	-0.0234 (± 0.0052)	2.31 (± 0.20)	0.14 (± 0.09)
Lin et al. (2012) ^a	267 (± 2)	127 (± 5)	5.1 (± 0.2)			
Lavina et al. (2009) ^b	263 (± 3)	148 (± 12)	5			

^a $(\text{Fe}_{0.65}\text{Mg}_{0.33}\text{Mn}_{0.02})\text{CO}_3$; ^b $(\text{Fe}_{0.72}\text{Mg}_{0.24}\text{Mn}_{0.03}\text{Ca}_{0.01})\text{CO}_3$

658

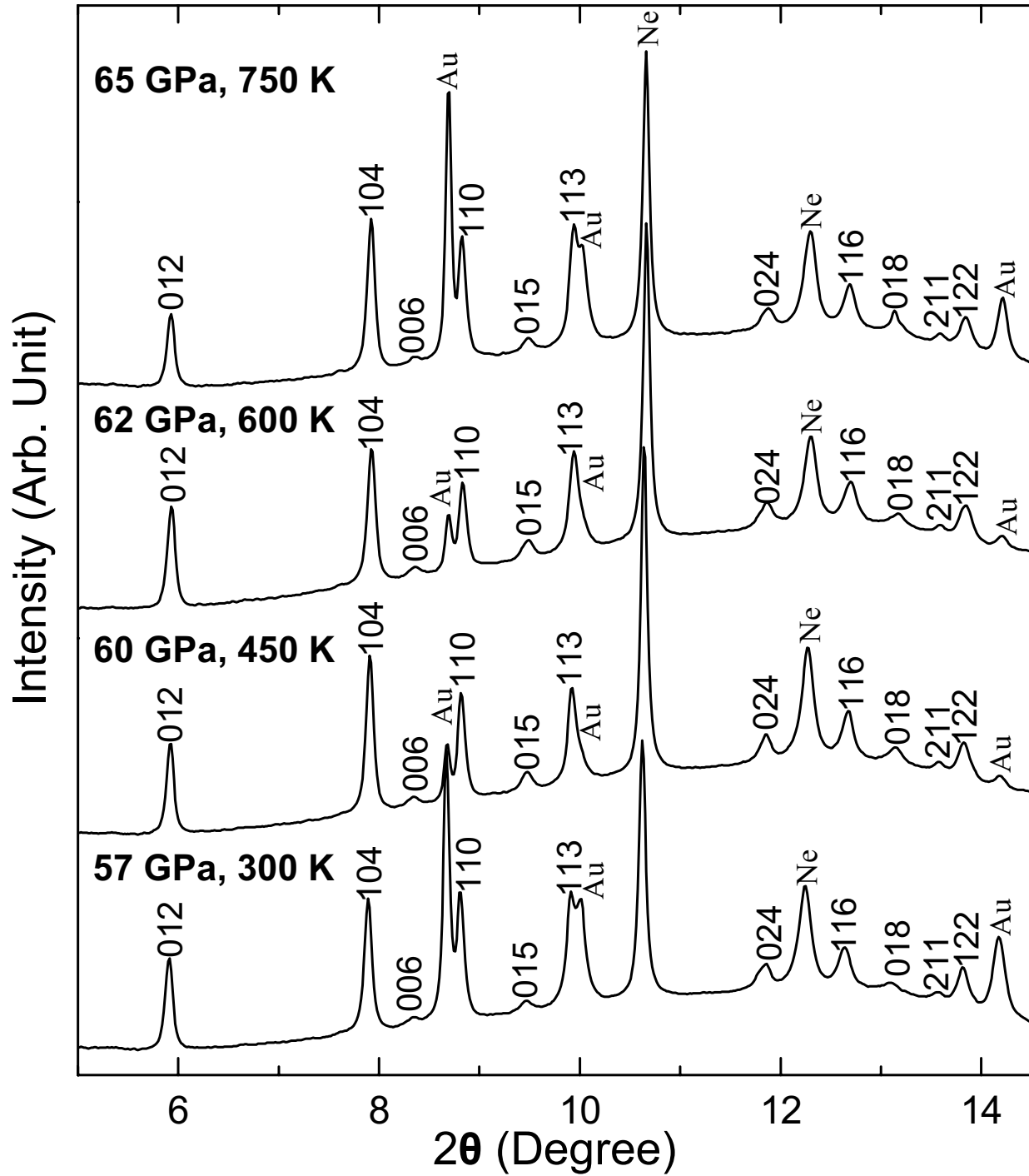


Figure 1

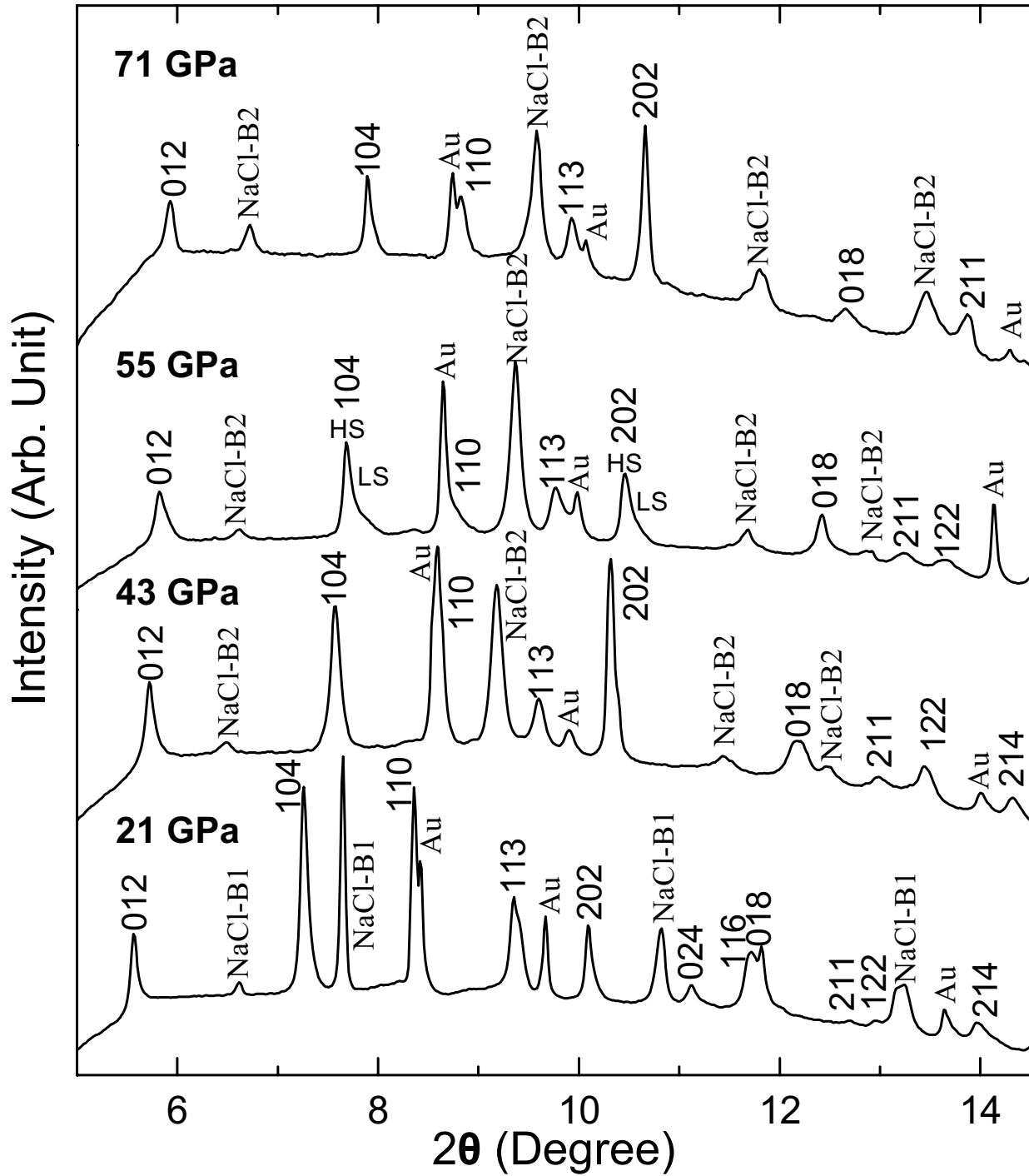


Figure 2

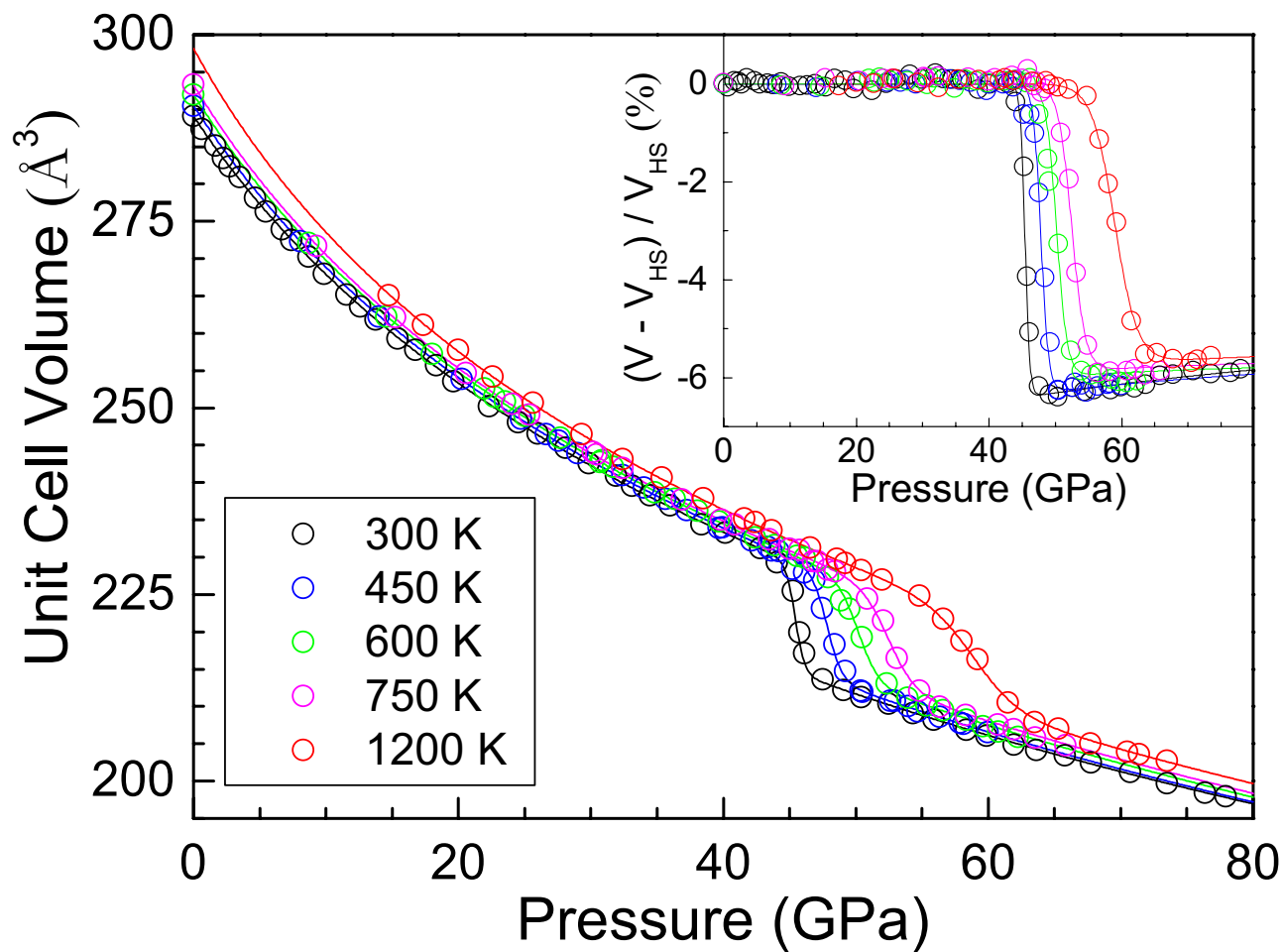


Figure 3

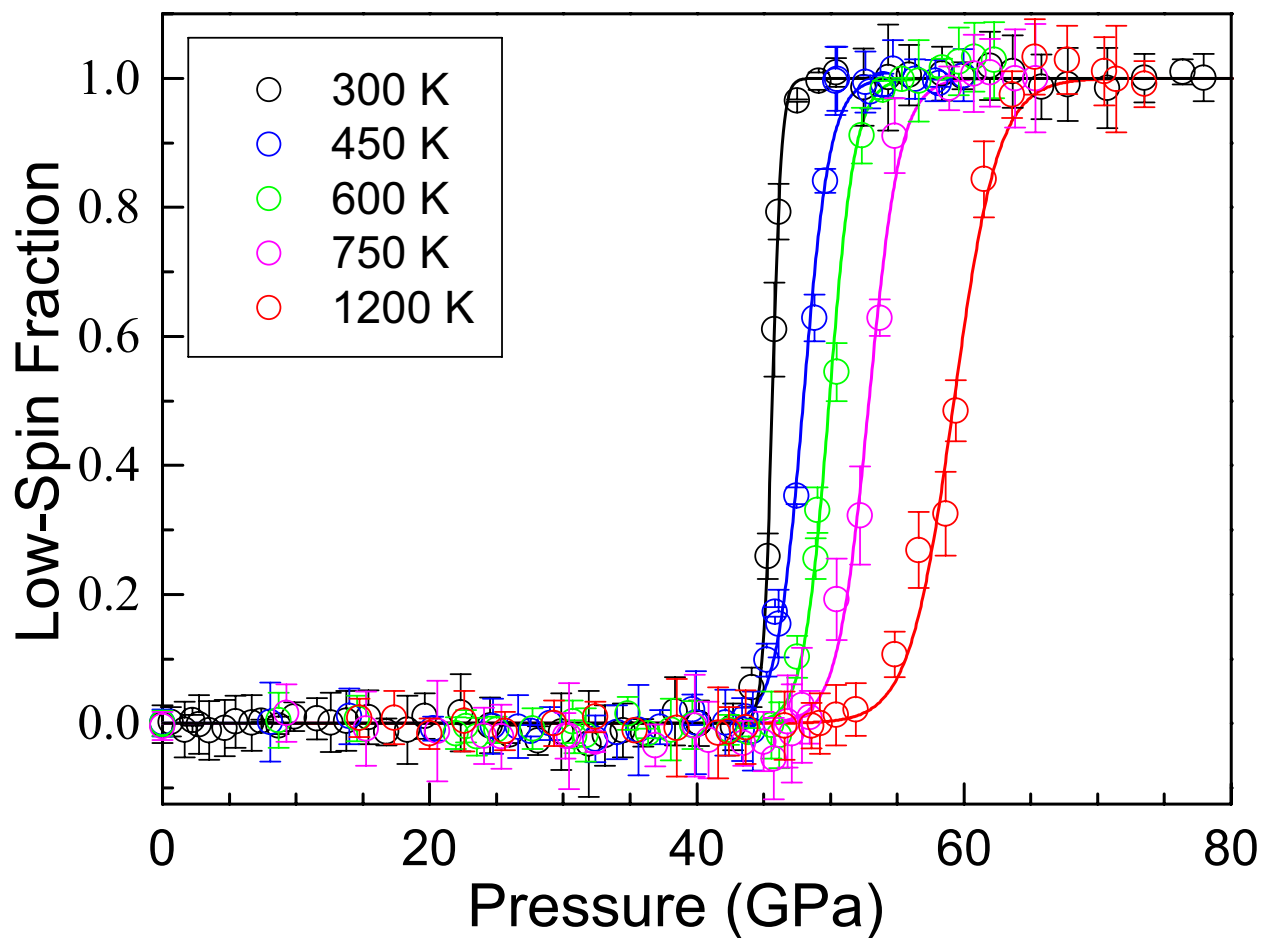


Figure 4

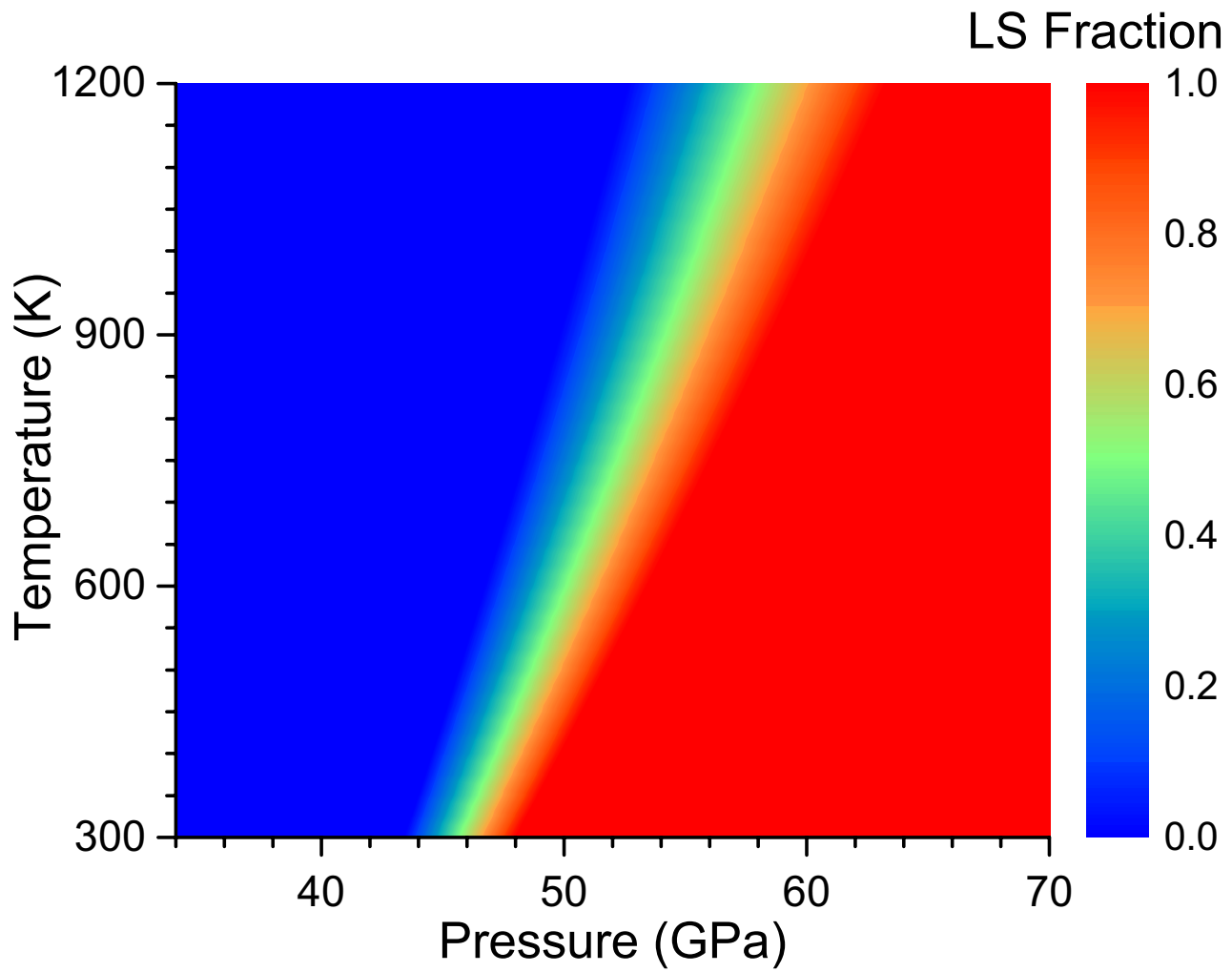


Figure 5

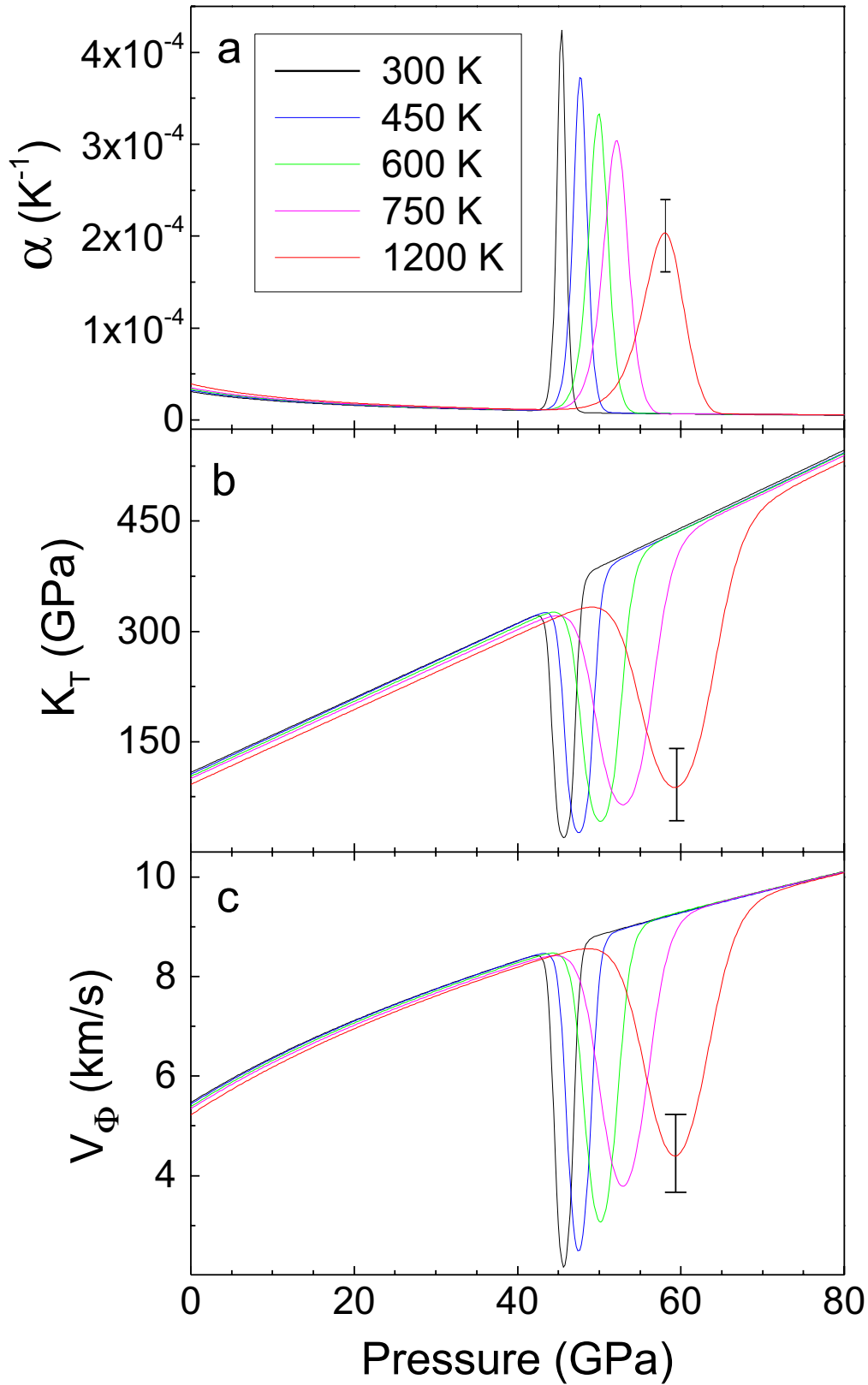


Figure 6

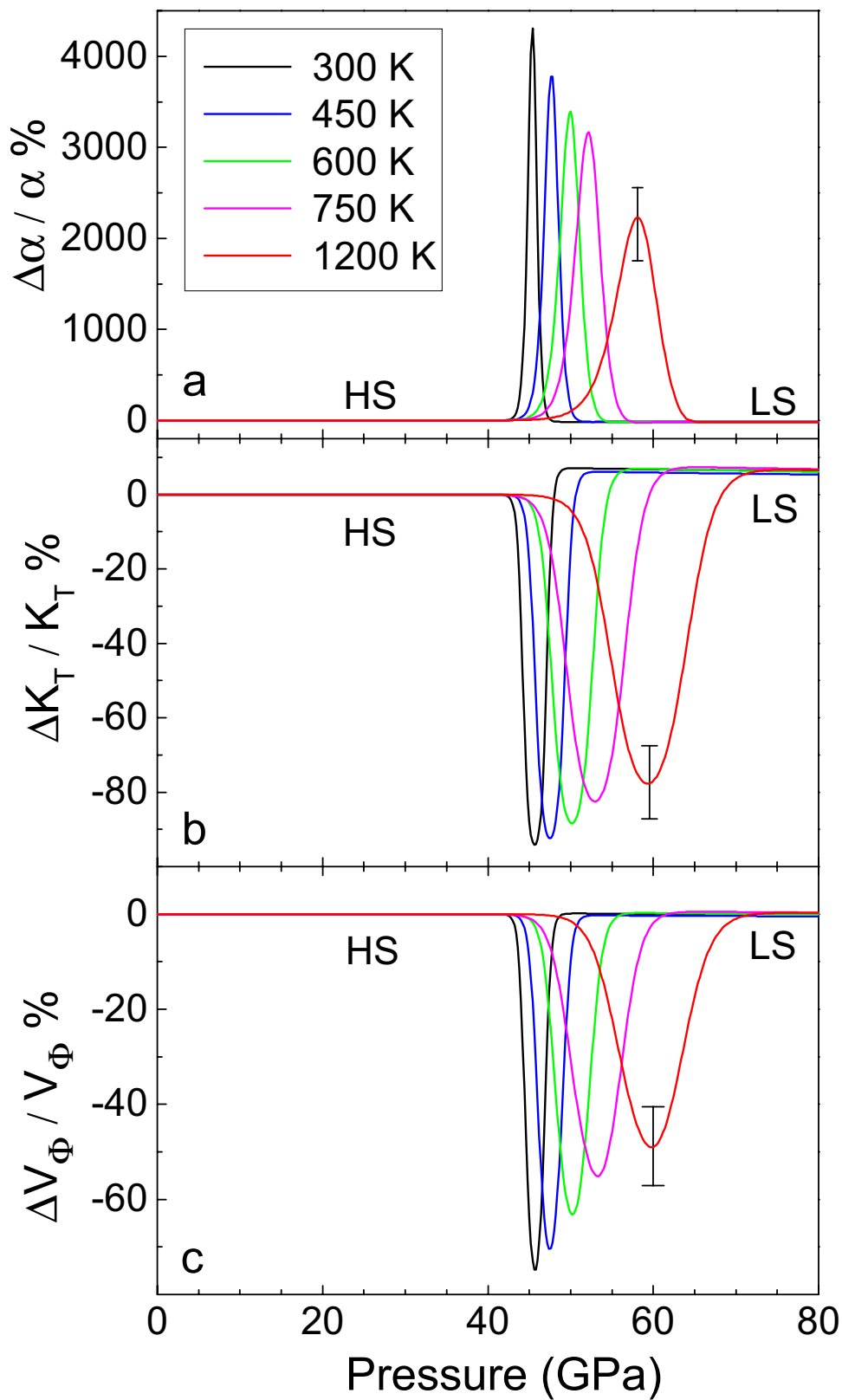


Figure 7

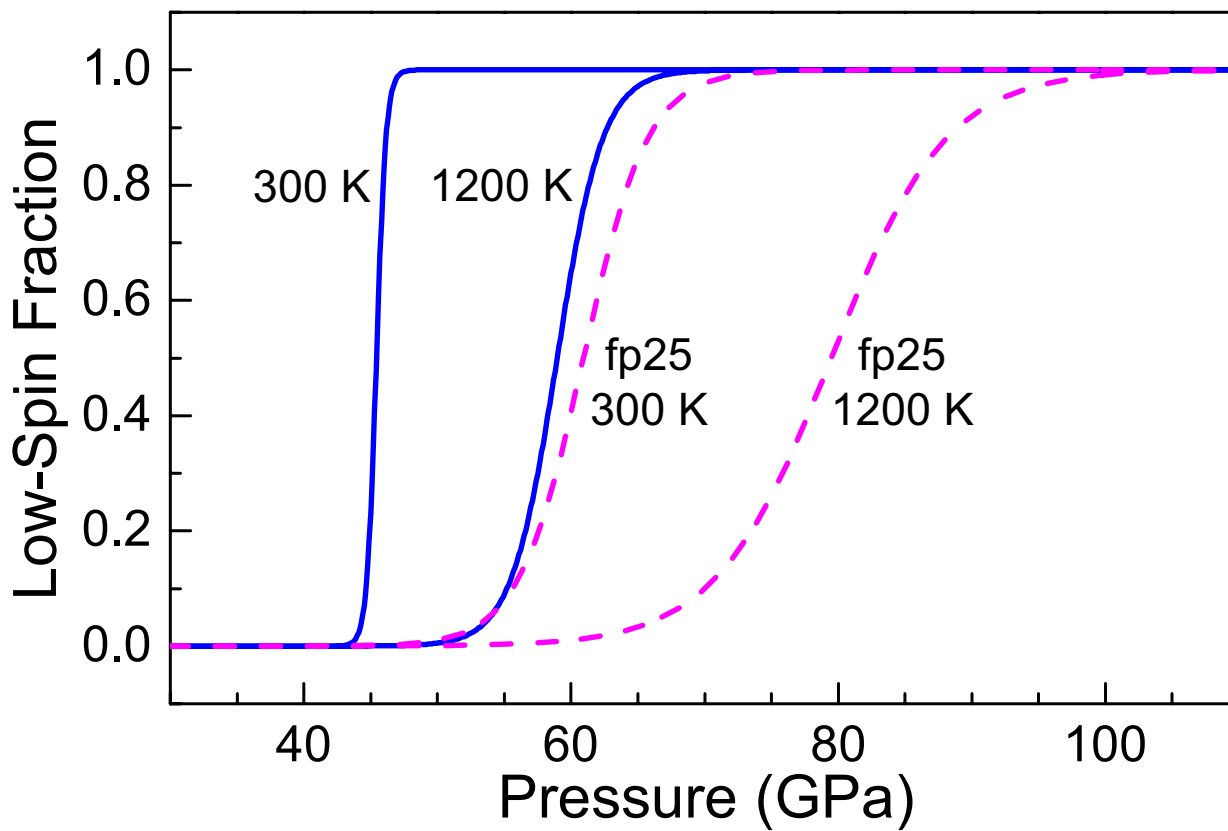


Figure 8

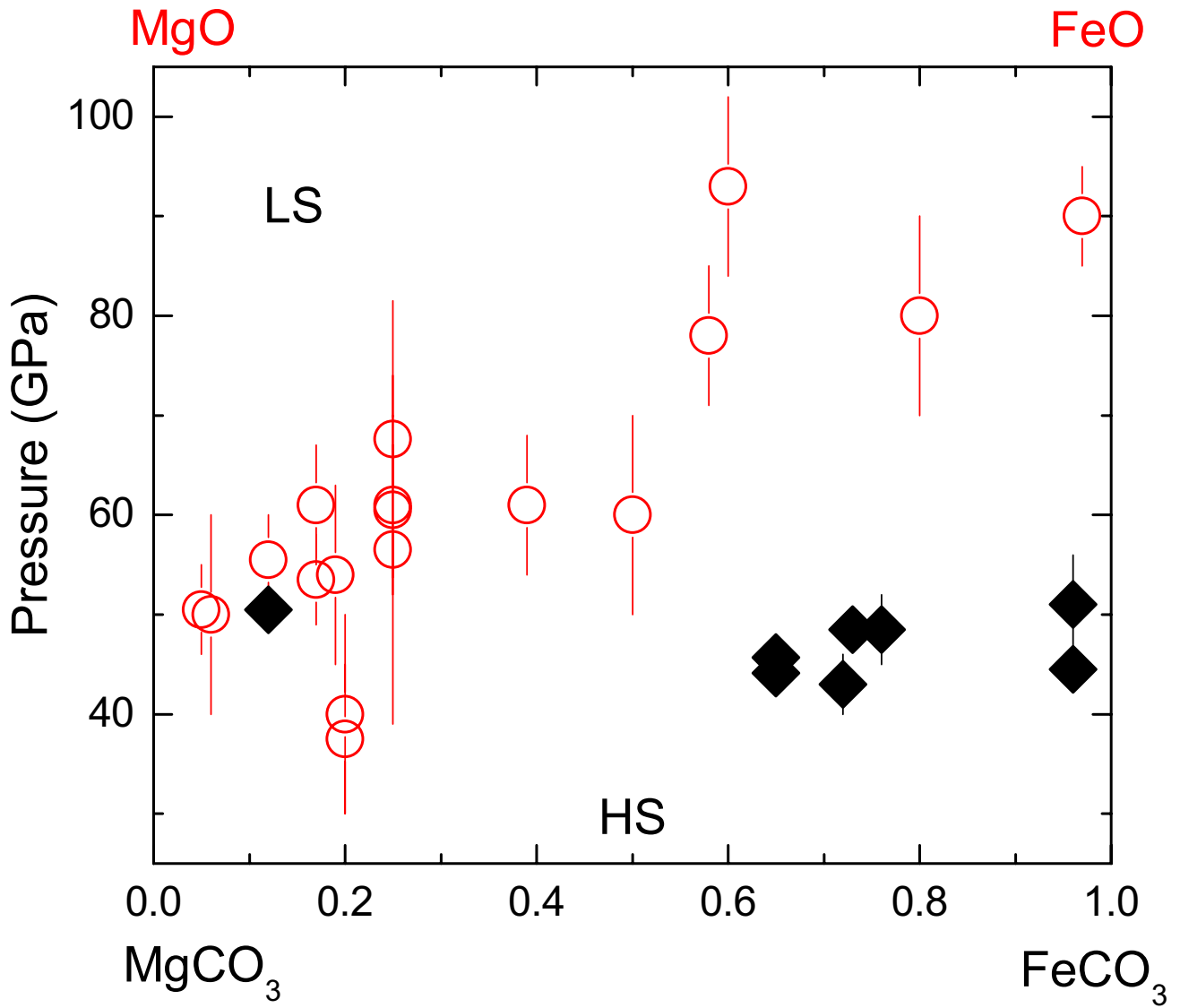


Figure 9

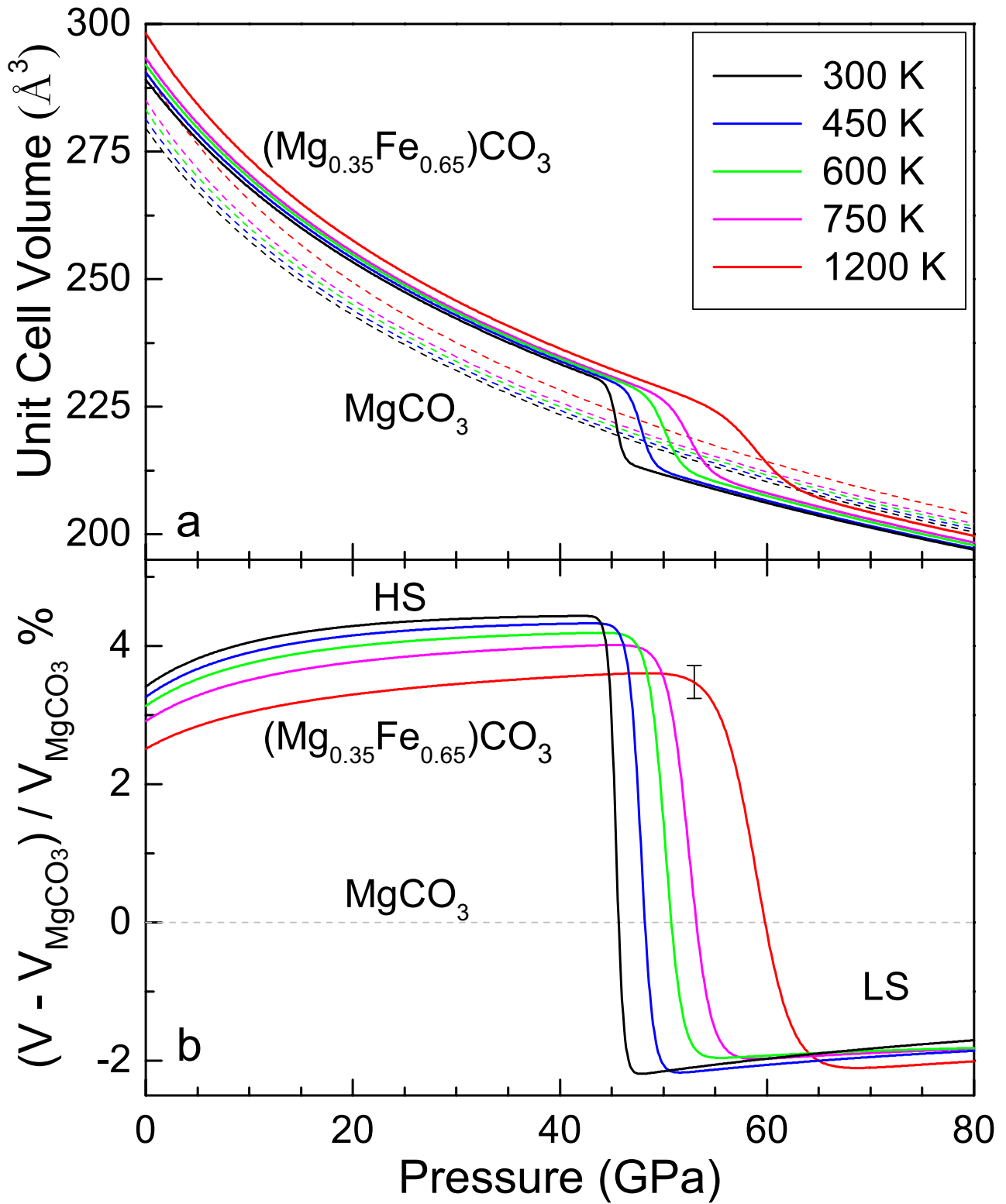


Figure 10

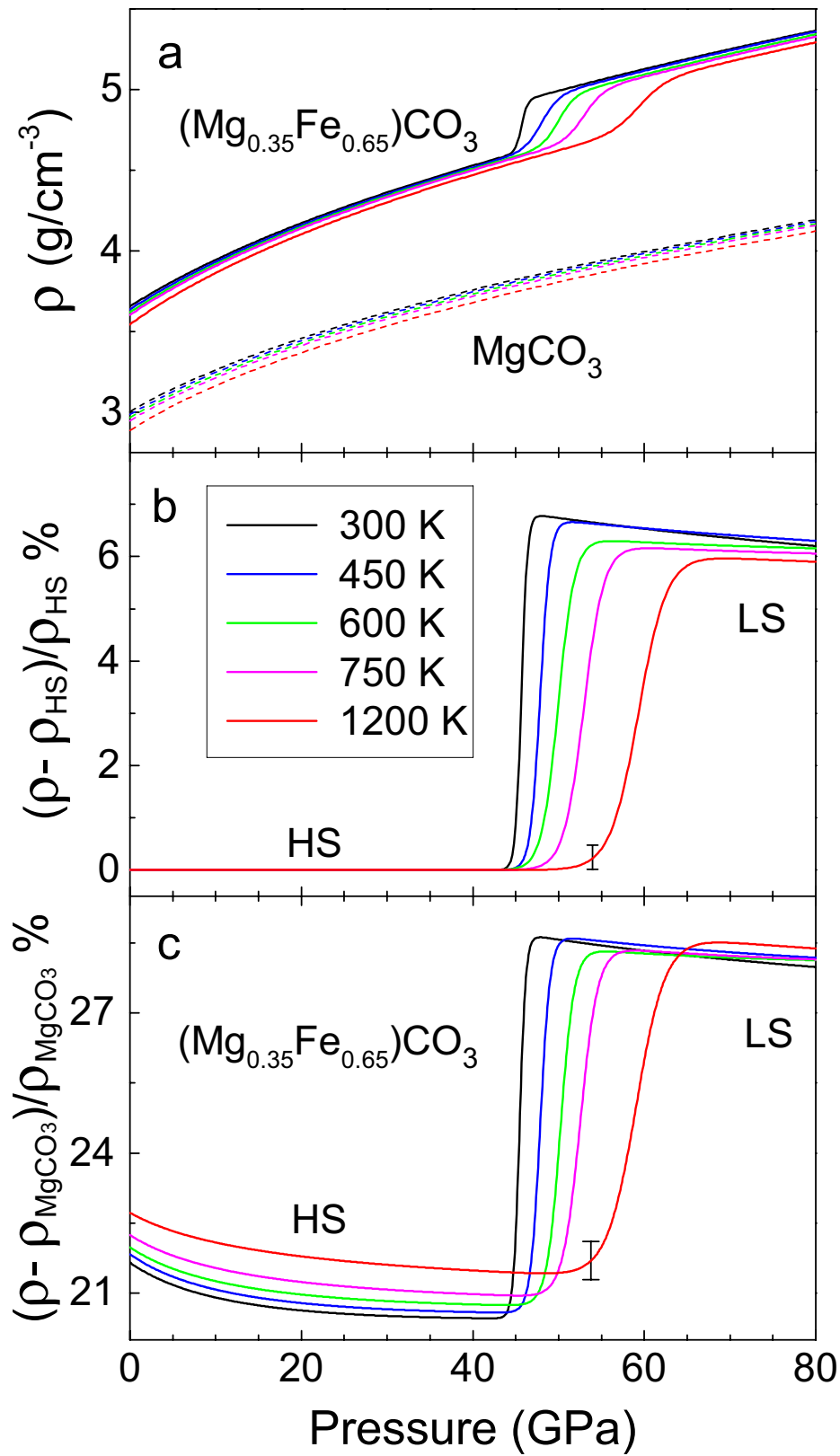


Figure 11